

Research Article

Synthesis and Characterization of Pyrochlore $\text{Bi}_2\text{Sn}_2\text{O}_7$ Doping with Praseodymium by Hydrothermal Method and Its Photocatalytic Activity Study

Weicheng Xu,¹ Guangyin Zhou,¹ Jianzhang Fang,¹ Zhang Liu,¹ YunFang Chen,¹ and Chaoping Cen²

¹ College of Chemistry and Environment, South China Normal University, Guangzhou 510631, China

² The Key Laboratory of Water and Air Pollution Control of Guangdong Province, South China Institute of Environmental Sciences, Guangzhou 510655, China

Correspondence should be addressed to Jianzhang Fang; fangjzh@scnu.edu.cn

Received 30 May 2013; Revised 15 July 2013; Accepted 15 July 2013

Academic Editor: Jiaguo Yu

Copyright © 2013 Weicheng Xu et al. This is an open access article distributed under the Creative Commons Attribution License, which permits unrestricted use, distribution, and reproduction in any medium, provided the original work is properly cited.

Praseodymium doped $\text{Bi}_2\text{Sn}_2\text{O}_7$ (BSO), as a visible-light responsive photocatalyst, was prepared by a hydrothermal method with different dopant contents. The as-prepared photocatalysts were investigated by X-ray diffraction (XRD), scanning electron microscope (SEM), transmission electron microscope (TEM), N_2 adsorption-desorption isotherm, X-ray photoelectron spectroscopy analysis (XPS), and UV-Vis diffuse reflectance spectroscopy (DRS). The photocatalytic activity of prepared catalysts was evaluated by the degradation of Rhodamine Bextra (RhB) and 2,4-dichlorophenol (2,4-DCP) in aqueous solution under visible light irradiation. It was found that Pr doping inhibited the growth of crystalline size and the as-prepared materials were small in size (10–20 nm). In our experiments, Pr-doped BSO samples exhibited enhanced visible-light photocatalytic activity compared to the undoped BSO, and the optimal dopant amount of Pr was 1.0 mol% for the best photocatalytic activity. On the basis of the calculated PL spectra, the mechanism of enhanced photocatalytic activity has been discussed.

1. Introduction

Semiconductor photocatalysis has been a very attractive research topic since its potential in the treatment of biorecalcitrant components in wastewaters [1, 2]. Among the semiconductors, TiO_2 has been widely discussed as a photocatalyst to purify air and water polluted with various hazardous chemicals due to its high photocatalytic activity, low cost, nontoxicity, and good stability [3, 4]. However, low quantum yields and the lack of visible-light utilization blocked its practical application. Therefore, much effort has been done in order to enhance the photocatalytic efficiency and visible-light utilization of TiO_2 , such as metal ion doping [5–7], nonmetal doping [8, 9], and coupling with other semiconductors [10]. In addition, the development of novel visible-light respond photocatalysts has been put forward and drawn great attention, such as $\text{Bi}_2\text{Ti}_2\text{O}_7$ [11, 12], $\text{La}_2\text{Zr}_2\text{O}_7$ [13], and $\text{Bi}_{1.5}\text{MgNb}_{1.5}\text{O}_7$ [14].

As a kind of pyrochlore-type composite oxides, bismuth pyrochlore ($\text{Bi}_2\text{Sn}_2\text{O}_7$) has received considerable attention by a number of groups due mainly to its demonstrated applications in catalysis and gas sensing [15–18]. Moens et al. [19] used $\text{Bi}_2\text{Sn}_2\text{O}_7$ (BSO) mechanically mixed with MoO_3 to evidence a cooperation catalytic effect between BSO and $\text{Bi}_2\text{Mo}_3\text{O}_{12}$. Kim et al. [20] utilized a novel method to prepare SnO_2 nanowires with BSO nanoparticles and investigated its oxygen sensing properties. Wu et al. [21] explored band engineering to improve visible light photocatalysis of nano-BSO. All previous research studies showed that it was necessary to take steps to promote the photocatalytic efficiency of pure BSO. Doping with rare earth ions also could reduce the recombination rate of electron-hole pairs and enhance the interfacial charge transfer efficiency [22], such as La-TiO_2 [23], Nd-TiO_2 [24], and $\text{Ce-Bi}_2\text{O}_3$ [25]. However, rare-earth doped BSO and its corresponding photocatalytic activity have been rarely investigated.

In the present work, in order to expand its absorption in visible light, the Pr-doping within the BSO photocatalyst was carried out by hydrothermal method. Furthermore, the effects of different Pr-doping amounts and the reasons accounting for the photocatalytic results were discussed. Meanwhile, the model pollutants of RhB and 2,4-CP were chosen to evaluate the photocatalytic activity of as-prepared photocatalysts under visible light irradiation.

2. Experimental

2.1. Synthesis. All chemicals were obtained commercially and used without further purification. $\text{Bi}(\text{NO}_3)_3 \cdot 5\text{H}_2\text{O}$ and $\text{K}_2\text{SnO}_3 \cdot 3\text{H}_2\text{O}$ were used as the starting materials for the syntheses. Pr-doped BSO was synthesized by hydrothermal method, and in every aqueous phase, dosage of 1.46 g of $\text{Bi}(\text{NO}_3)_3 \cdot 5\text{H}_2\text{O}$ (3 mmol) and 0.9 g of $\text{K}_2\text{SnO}_3 \cdot 3\text{H}_2\text{O}$ (3 mmol) was added to 80.0 mL of deionized water and then mixed with $\text{Pr}(\text{NO}_3)_3 \cdot 6\text{H}_2\text{O}$ according to the doping ratio of Pr/BSO of 0, 0.5, 1.0, 2.0, and 3.0 mol%, respectively. Under vigorous stirring, the pH value of the mixture was adjusted to 12 by using 2 mol/L KOH. After the solids were completely dissolved in the solution at room temperature, the autoclave was sealed, heated under autogenous pressure at 180°C for 24 h, and then cooled down to room temperature naturally. The resultant precipitates were filtered, washed with deionized water and anhydrous ethanol, and then dried in a vacuum oven at 60°C for 12 h. The final products were milled using an agate mortar before characterization. The samples were labeled as $x\%$ -Pr-BSO, where $x\%$ was the molar ratio of Pr to BSO.

2.2. Characterization. The as-prepared samples were characterized by powder X-ray diffraction (XRD) instrument (Bruker D8 ADVANCE). The scanning electron microscopy (SEM) images were obtained on a JEOL JSM 6700F instrument with an accelerating voltage of 20 kV. Transmission electron micrographs (TEM) images were recorded using a JEM-2100HR (JEOL, Japan) microscope at an accelerating voltage of 200 kV. X-ray photoelectron spectroscopy (XPS) analysis was performed on an ESCALAB 250 photoelectron spectroscopy (Thermo-VG Scientific) at 2.0×10^{-10} mbar using Al $K\alpha$ X-ray beam (1486.6 eV). UV-Vis diffuse reflectance spectrum (DRS) was determined on a Hitachi U-3010 UV-Vis spectrophotometer with BaSO_4 as the background between 250 and 800 nm. The BET surface area and pore volume of samples were measured by a Micromeritics ASAP 2010 nitrogen adsorption apparatus. The photoluminescence (PL) spectra of photocatalysts were recorded by a fluorescence spectrophotometer (Shimadzu Rf-540, Japan) using a 150 W xenon lamp as light source.

2.3. Photocatalytic Activity Measurement. RhB and 2,4-DCP were adopted as a representative organic pollutant to evaluate the photocatalytic activity of as-prepared samples under visible light irradiation. All photocatalytic experiments were conducted at room temperature. The catalyst (0.1g) was immersed in a 250 mL Pyrex beaker with 100 mL of RhB

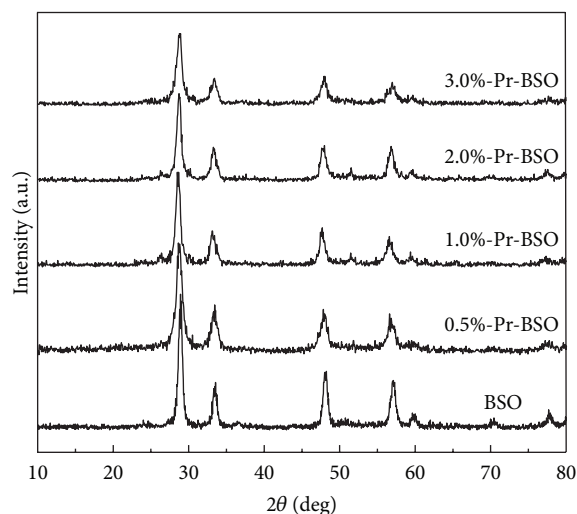


FIGURE 1: XRD analysis of different Pr-doped photocatalysts.

solution (5 mg/L) or 2,4-DCP solution (20 mg/L). The suspensions were magnetically stirred in the dark for 40 min prior to irradiation to achieve adsorption-desorption equilibrium on the catalysts surface at room temperature. As for the photocatalytic reactions, a 300 W Xe arc lamp (LTIC 300BF, BoYi Ltd., China), with a 420 nm cut-off filter, was provided about 10 cm from the top surface of the suspensions, and the concentration of pollutants during photocatalysis was monitored by pulling out about 5.0 mL suspension periodically from the reactor and centrifuging for analysis. A UV-vis 8500 spectrophotometer (Shanghai Tianmei Science Apparatus Ltd., Co., China) was used to analyse the RhB and the high performance liquid chromatography (HPLC, Shimadzu) was assisted to determine the degradation of 2,4-DCP.

3. Results and Discussion

3.1. Phase Structure and Morphology of the As-Prepared Samples. BSO has three polymorphs (monoclinic α , face-centered cubic β , and cubic pyrochlore γ) [17], and the thermodynamically stable phase is α -BSO. In this paper, γ -BSO is obtained by a hydrothermal method. The powder XRD patterns of different Pr-doped BSO photocatalysts are presented in Figure 1. The XRD of samples shows several strong peaks at $2\theta = 28.8^\circ, 33.4^\circ, 47.9^\circ,$ and 56.9° , which represent the formation of pyrochlore structure. The diffraction peaks of pure BSO and the doped samples are similar and are found to be in a good agreement with the standard XRD patterns of cubic pyrochlore (JCPDS no. 87-0284). In terms of Pr-doped BSO, the peak at 28.8° corresponding to characteristic peak of the crystal plane (222) becomes broader and the relative intensity decreases with increasing Pr ion dosage. On the basis of the Scherrer equation, the average size of crystallite is calculated from the (222) peak of pyrochlore BSO. The results are summarized in Table 1, and the crystallite size decreased with increasing the amount of praseodymium. It can be attributed to the segregation of the praseodymium cations at the grain boundary, which inhibited the grain growth by restricting direct contact of grains [26].

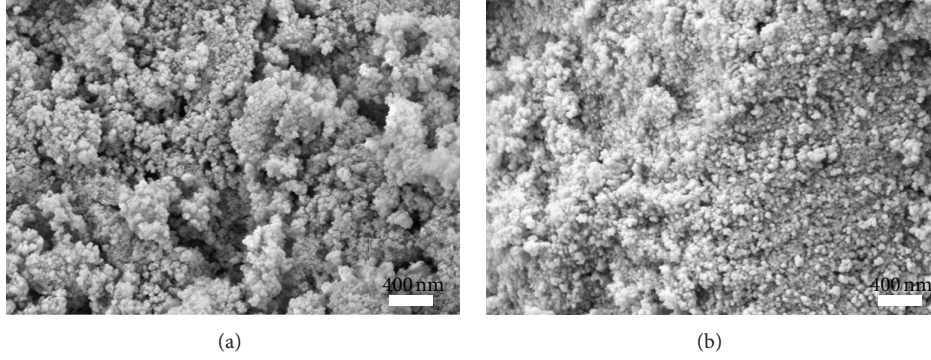


FIGURE 2: SEM images of as-prepared samples: (a) BSO sample and (b) 1%-Pr-BSO sample.

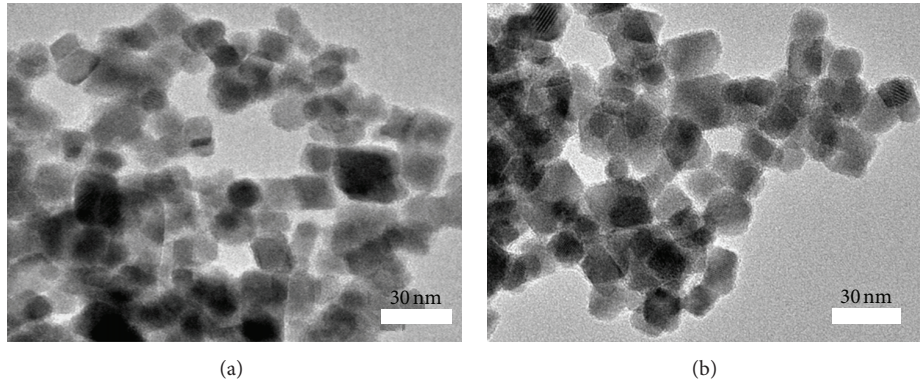


FIGURE 3: TEM images of (a) BSO sample and (b) 1%-Pr-BSO sample.

TABLE 1: Crystallite size, BET surface areas, and pore size of different photocatalysts.

Sample	Crystallite size $D(222)$ (nm)	S_{BET} (m^2/g)	Pore size (nm)
Pure BSO	13.5	45.3	9.4
0.5%-Pr-BSO	12.5	52.4	9.1
1.0%-Pr-BSO	11.3	61.6	8.1
2.0%-Pr-BSO	10.6	59.3	8.5
3.0%-Pr-BSO	9.8	54.7	8.8

Figure 2 shows the typical SEM images of pure BSO and 1.0%-Pr-BSO. As seen from the SEM micrograph, a large number of small particles are presented in Figure 2(a) (BSO) and Figure 2(b) (1.0%-Pr-BSO), demonstrating that high yield of products can be readily achieved through this approach. The diameters of particles that consisted of spherical clusters are around 8–20 nm.

Figures 3(a) and 3(b) show the TEM photograph of BSO and 1.0%-Pr-BSO, respectively. From Figure 3(a), it can be seen that BSO nanoparticles have irregular lump-like and spherical-like morphology, and the diameter is about 8–20 nm. However, 1.0%-Pr-BSO with a thin layer of about 2 nm in thickness has smaller grain size than BSO, which is consistent well with that calculated from the XRD data (Table 1).

3.2. N_2 Adsorption/Desorption Isotherm Analysis. The specific surface areas and pore size distributions of the BSO

and 1.0%-Pr-BSO are measured using nitrogen gas sorption. The nitrogen adsorption-desorption isotherms of BSO (Figure 4(a)) and 1.0%-Pr-BSO (Figure 4(b)) exhibit stepwise adsorption and desorption (type-IV isotherm), indicating that the samples have mesoporous structure [26]. The specific surface area of BSO is $45.3 \text{ m}^2/\text{g}$, but after Pr coating, the BET surface area of 1.0%-Pr-BSO is increased to $61.6 \text{ m}^2/\text{g}$. High specific surface area of 1.0%-Pr-BSO will provide more active site for the photocatalytic reaction and enhance the interfacial reaction process. The pore size distribution plots of as-prepared samples calculated using the BJH equation from the absorption branch of the isotherm are shown in the inset of Figure 4. The result suggests that the spherical BSO sample has pronounced mesoporosity of narrow pore size distribution with average pore diameter around 12 nm. The specific surface area and pore diameter are calculated and also listed in Table 1.

3.3. X-Ray Photoelectron Spectroscopy Analysis. 1.0%-Pr-BSO is analyzed by XPS to discuss the elemental composition and chemical state on the BSO surface. The XPS survey spectrum is shown in Figure 5(a). It can be seen that 1.0%-Pr-BSO contains only five elements, namely, Bi, Sn, O, Pr, and C. Carbon probably originates from the calcinations residue of the precursor and adventitious hydrocarbon from the XPS instrument itself. In Bi 4f XPS spectrum (Figure 5(b)), two symmetric peaks at 164.3 eV and 159.1 eV, assigned to Bi 4f_{5/2} and Bi 4f_{7/2}, correspond to Bi⁴⁺ and Bi³⁺, respectively [27].

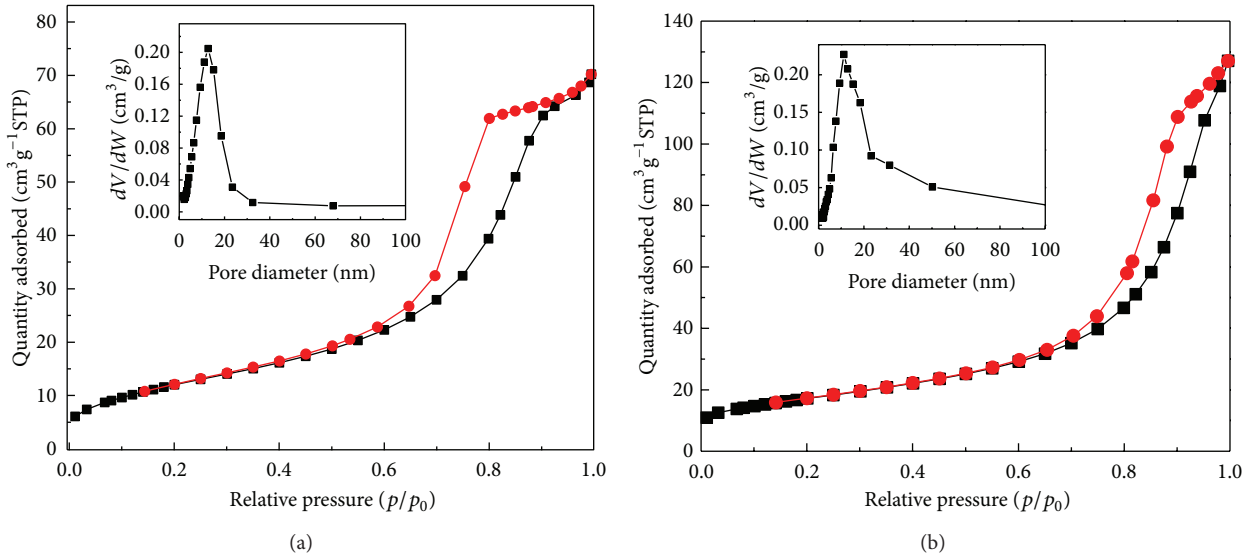


FIGURE 4: The N_2 sorption isotherms and pore size distribution of (a) BSO and (b) 1%-Pr-BSO.

TABLE 2: Maximum absorption and band gap of as-prepared samples.

Sample	Maximum absorption (nm)	Band gap (eV)
BSO	450	2.76
0.5%-Pr-BSO	436	2.84
1.0%-Pr-BSO	460	2.70
2.0%-Pr-BSO	422	2.94
3.0%-Pr-BSO	436	2.84

From the high resolution XPS spectra, it can be observed that the binding energies of Sn $3d_{5/2}$ and O 1s are 486.8 eV and 530.4 eV, respectively. Moreover, the binding energies of Sn $3d_{5/2}$ and O 1s are consistent with the literature values for Sn⁴⁺ and O⁻ in BSO [28, 29]. Figure 5(e) shows that the peaks of Pr $3d_{5/2}$ and Pr $3d_{3/2}$ are located at 933.7 eV and 953.5 eV. The results mean that the Pr oxidation state shows the presence of Pr³⁺ [21].

3.4. UV-Vis Diffuse Reflectance Spectra. Figure 6 displays UV-Vis diffuse reflection spectrum (DRS) of BSO precursors and Pr-BSO samples with different Pr contents. Figure 6(a) shows a phenomenon that the maximum absorptions of Pr-BSO photocatalysts, except the 1.0%-Pr-BSO sample, are slightly shifted to a shorter wavelength compared to those of pure BSO. The red shift of the absorption edge in 1.0%-Pr-BSO has been attributed to the charge-transfer transition between Pr ion f electrons and the BSO conduction or valence band [24]. As it is shown in Figure 6(b), the band gap achieved by extrapolation in 1.0%-Pr-BSO (460 nm) at the meeting point of the two tangents is about 2.70 eV. The maximum absorption wavelength and band gap of other photocatalysts are displayed in Table 2.

3.5. Photocatalytic Activity. To evaluate the photocatalytic activity of BSO and Pr-BSO with different molar ratios,

the photodegradation of RhB and 2,4-DCP is carried out in aqueous dispersions under visible light illumination (Figure 7). In order to ensure adsorption/desorption equilibrium, adsorption experiments are carried out on all samples in the dark for 40 min. From Figure 7, it can be observed that the doped samples have a higher absorption rate compared with that of the undoped BSO. So it is obvious that Pr ions benefit the adsorption processes. When the BSO nanoparticles are modified by Pr ions, the Pr-BSO photocatalysts show an obvious enhanced photocatalytic activity and model pollutants (RhB and 2,4-DCP) are quickly decomposed with increasing irradiation time. After visible-light irradiation for 4 h, the degradation of RhB and 2,4-DCP over pure BSO reaches 52.0% and 50.2%, respectively. However, 90.8% of RhB and 87.6% of 2,4-DCP are degraded in 4 h irradiation over 1.0%-Pr-BSO. In this experiment, 1.0 mol% praseodymium is the optimal dopant content. It is found that the photocatalytic activity increased with increasing Pr loading to the optimum value and then decreased with further increase of Pr content. This result can be attributed to the influence of the space charge layer thickness [30]. As the doped contents are low, the surface barrier becomes higher and the space charge region becomes narrower, and at last the electron-hole pairs are efficiently separated before recombination. However, when the doped content is above its optimum, the space charge region becomes very narrow and the penetration depth of light into photocatalysts greatly exceeds the space charge layer, so that the electron and hole pairs recombine easily. Consequently, there is an optimum concentration of Pr ions.

3.6. Visible Light Photodegradation Mechanism. According to many previous investigations on the mechanism of photocatalytic degradation, it is widely confirmed that hydroxyl radicals ($\cdot\text{OH}$) are a key active species in the photocatalytic process [31, 32]. It can attack the adsorbed toxic organic molecules to produce oxidized species and/or

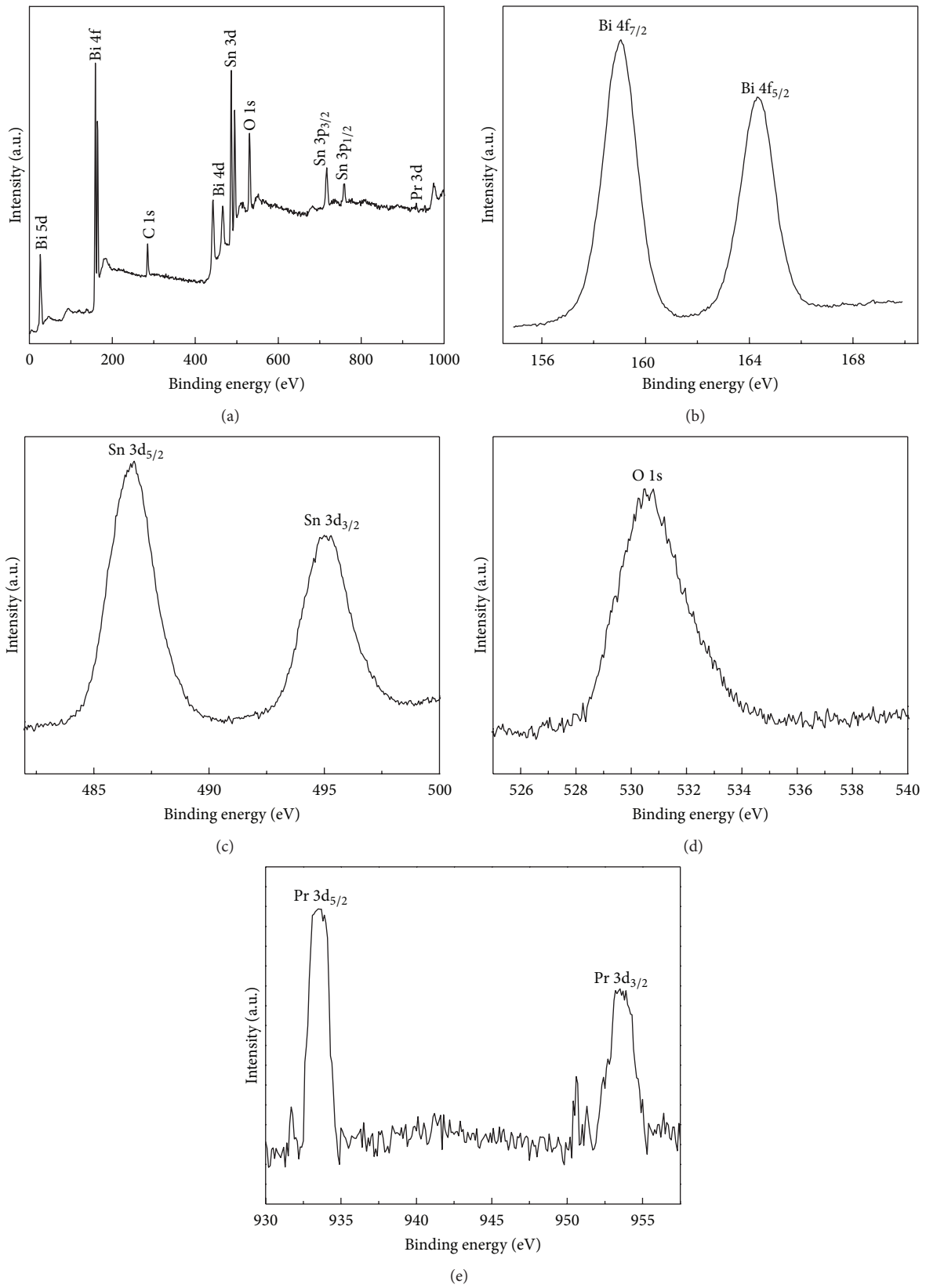


FIGURE 5: XPS spectra of 1%-Pr-BSO sample: (a) survey spectrum, (b) Bi 4f, (c) Sn 3d, (d) O 1s, and (e) Pr 3d.

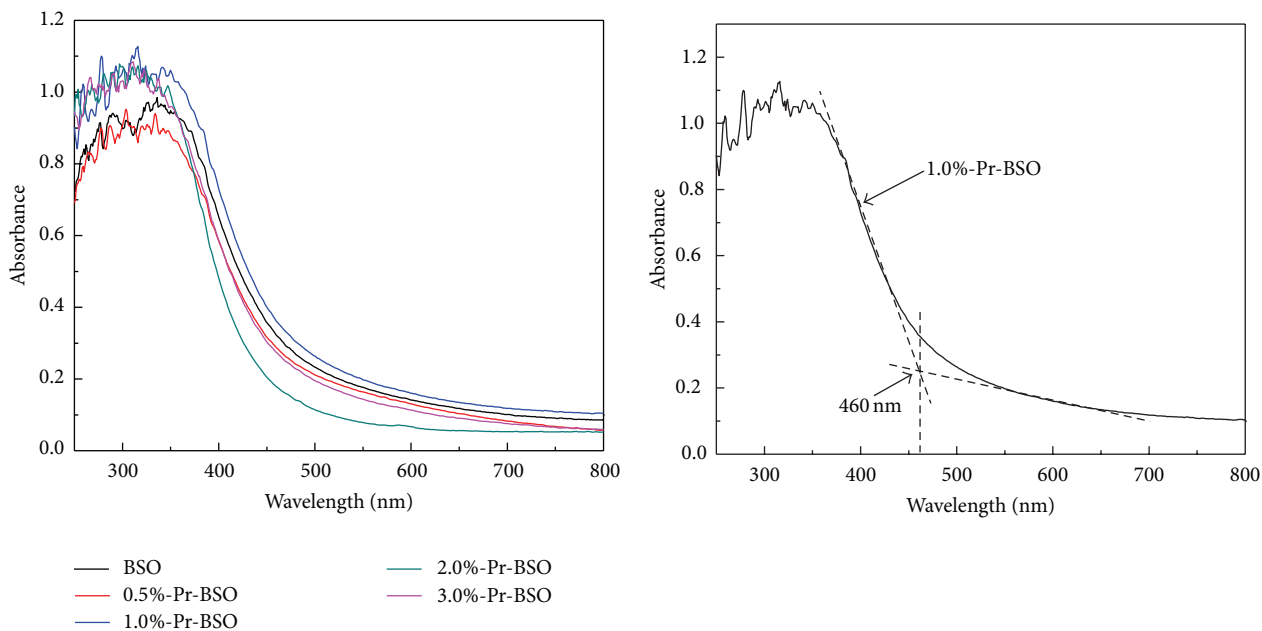


FIGURE 6: UV-Vis diffuse reflectance spectra of (a) different Pr-doped BSOs and (b) 1%-Pr-BSO.

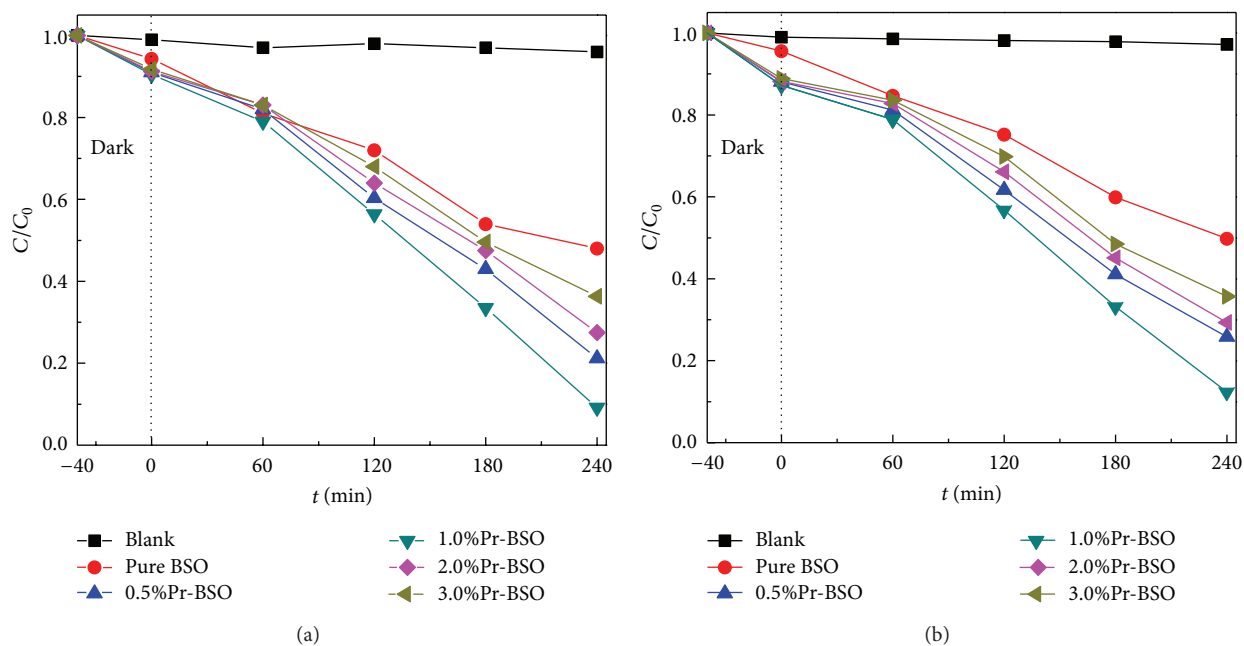


FIGURE 7: Degradation curves of (a) RhB and (b) 2,4-DCP.

decomposed products [33]. The analysis of $\cdot\text{OH}$ radical is performed by fluorescence technique using terephthalic acid, which can react with $\cdot\text{OH}$ radical in basic solution and generate 2-hydroxy terephthalic acid (TAOH) [34]. TAOH emits a strong fluorescence signal at around 426 nm on the excitation of its own 312 nm absorption band. Therefore, the formation of $\cdot\text{OH}$ radicals at the photocatalytic system was detected by PL technique using terephthalic acid as a probe molecule. Figure 8(a) shows the fluorescence spectra

of 1%-Pr-BSO catalyst recorded at the same interval of irradiation time. It was obvious that the photoluminescence emission peak at about 426 nm was continuously enhanced. However, no fluorescence emission was observed in the absence of visible light. Figure 8(b) shows the plot of increase in fluorescence intensity against illumination time at 426 nm. The fluorescence intensity by visible light illumination in terephthalic acid solutions increased linearly against time. Based on the results, we could conclude that the large amount

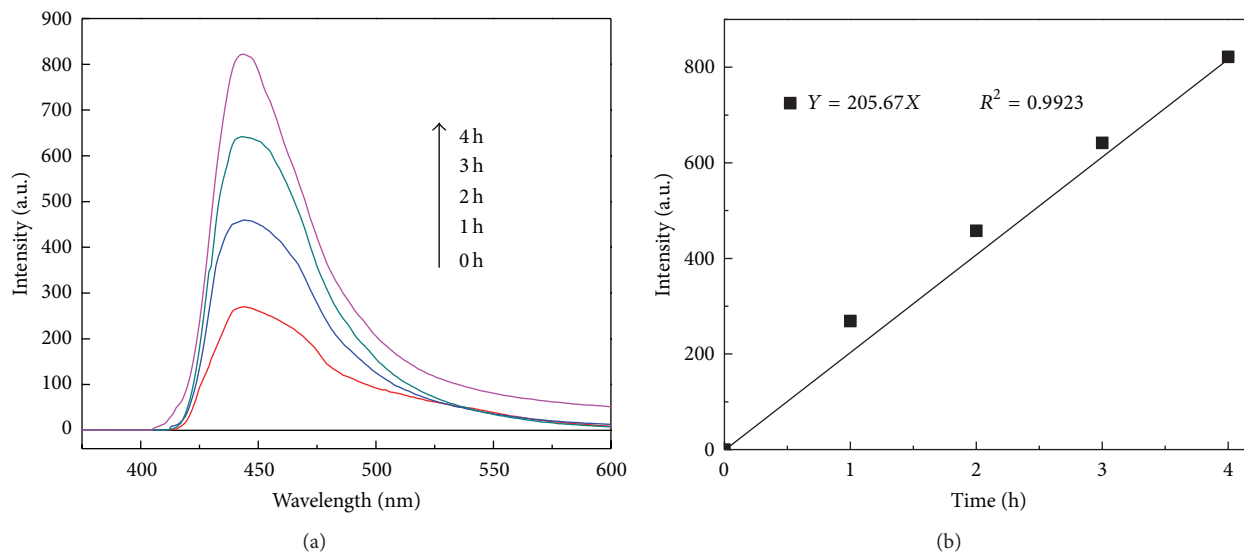


FIGURE 8: (a) $\cdot\text{OH}$ -trapping photoluminescence spectra of 1%-Pr-BSO in solution of terephthalic acid at room temperature (ex, 312 nm; em, 426 nm) and (b) plots of the induced PL intensities of 1%-Pr-BSO at 426 nm on the irradiation time.

of $\cdot\text{OH}$ was generated in the 1%-Pr-BSO photocatalytic system under visible light irradiation. The generation of $\cdot\text{OH}$ radicals was the main active species in the photocatalytic system.

3.7. Discussion on Photocatalysis Process of Pr-BSO. Generally, the photoexcited state of Pr cations is generated by the absorption of light, corresponding to the transition of the electrons situated in the inner 4f orbital to the 4s orbital [35]. The excited state ions have the capability of transferring their excited energy to other adsorbed molecules (f-f transition) [36]. The transitions of 4f electrons can lead to the enforcement of the optical adsorption of catalysts [24]. Reddy et al. [37] reported that rare earth elements could be used as good electron acceptors, and it could capture excited electron and facilitate the separation of electron-hole pairs. As we all know, photons from visible irradiation are used to generate electrons and holes. The holes react with H_2O or OH^- to form hydroxyl radicals ($\cdot\text{OH}$) and the electron-hole separation process is improved because BSO sample transfers photoelectrons to Pr when praseodymium appears on BSO surface [22, 30]. Subsequently, the electrons migrate from Pr to the adsorbed O_2 to form $\text{O}_2^{\cdot-}$. $\cdot\text{OH}$ and $\text{O}_2^{\cdot-}$ are important species which possess strong capability of oxidizing and breaking RhB and 2,4-DCP in aqueous solution [25]. The photocatalytic procedure is presented in Figure 9.

4. Conclusions

Pr-doped BSO materials prepared by a facile hydrothermal method were successfully used in the photocatalytic conversion of RhB and 2,4-DCP under visible light. The nanostructured Pr-BSO samples possessed high photocatalytic activity, fine-grained distribution and large surface area. The praseodymium doping effectively shifted the BSO

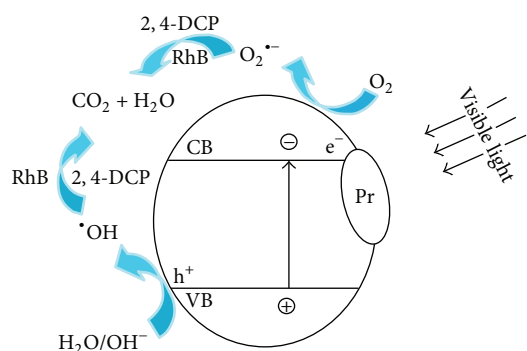


FIGURE 9: Photocatalysis process of Pr-doped BSO photocatalyst under visible light irradiation.

absorption edge and retarded the growth of crystallite. The as-prepared Pr-BSO photocatalysts displayed approximately the spherical shape and owned the mesoporous surface. An optimal Pr doping concentration existed and was 1.0 mol%, and superfluous Pr would make negative influence on photodegradation efficiency.

Acknowledgment

This work was supported by Guangdong Water and Air Pollution Control Key Laboratory (2011 A060901002) open funded project.

References

- [1] A. M. Ali, E. A. C. Emanuelsson, and D. A. Patterson, "Photocatalysis with nanostructured zinc oxide thin films: the relationship between morphology and photocatalytic activity under oxygen limited and oxygen rich conditions and evidence

- for a Mars Van Krevelen mechanism," *Applied Catalysis B: Environmental*, vol. 97, no. 1-2, pp. 168–181, 2010.
- [2] I. Bouzaida, C. Ferronato, J. M. Chovelon, M. E. Rammah, and J. M. Herrmann, "Heterogeneous photocatalytic degradation of the anthraquinonic dye, Acid Blue 25 (AB25): a kinetic approach," *Journal of Photochemistry and Photobiology A: Chemistry*, vol. 168, no. 1-2, pp. 23–30, 2004.
 - [3] Z. Liu, Z. Jian, J. Fang, X. Xu, X. Zhu, and S. Wu, "Low-temperature reverse microemulsion synthesis, characterization, and photocatalytic performance of nanocrystalline titanium dioxide," *International Journal of Photoenergy*, vol. 2012, Article ID 702503, 8 pages, 2012.
 - [4] J. Choi, H. Park, and M. R. Hoffmann, "Effects of single metal-ion doping on the visible-light photoreactivity of TiO₂," *Journal of Physical Chemistry C*, vol. 114, no. 2, pp. 783–792, 2010.
 - [5] M. Zhou, J. Zhang, B. Cheng, and H. Yu, "Enhancement of visible-light photocatalytic activity of mesoporous Au-TiO₂ nanocomposites by surface plasmon resonance," *International Journal of Photoenergy*, vol. 2012, Article ID 532843, 10 pages, 2012.
 - [6] H. Znad, M. H. Ang, and M. O. Tade, "Ta/TiO₂- and Nb/TiO₂-mixed oxides as efficient solar photocatalysts: preparation, characterization, and photocatalytic activity," *International Journal of Photoenergy*, vol. 2012, Article ID 548158, 9 pages, 2012.
 - [7] J. Yu, Q. Xiang, and M. Zhou, "Preparation, characterization and visible-light-driven photocatalytic activity of Fe-doped titania nanorods and first-principles study for electronic structures," *Applied Catalysis B: Environmental*, vol. 90, no. 3-4, pp. 595–602, 2009.
 - [8] N. Lu, X. Quan, J. Li, S. Chen, H. Yu, and G. Chen, "Fabrication of boron-doped TiO₂ nanotube array electrode and investigation of its photoelectrochemical capability," *Journal of Physical Chemistry C*, vol. 111, no. 32, pp. 11836–11842, 2007.
 - [9] J. Qian, G. Cui, M. Jing, Y. Wang, M. Zhang, and J. Yang, "Hydrothermal synthesis of nitrogen-doped titanium dioxide and evaluation of its visible light photocatalytic activity," *International Journal of Photoenergy*, vol. 2012, Article ID 198497, 6 pages, 2012.
 - [10] M. Sun, G. Chen, Y. Zhang, Q. Wei, Z. Ma, and B. Du, "Efficient degradation of azo dyes over Sb₂S₃/TiO₂ heterojunction under visible light irradiation," *Industrial and Engineering Chemistry Research*, vol. 51, no. 7, pp. 2897–2903, 2012.
 - [11] J. Ren, G. Liu, Y. Wang, and Q. Shi, "A novel method for the preparation of Bi₂Ti₂O₇ pyrochlore," *Materials Letters*, vol. 76, pp. 184–186, 2012.
 - [12] X. Lin, P. Lv, Q. Guan, H. Li, H. Zhai, and C. Liu, "Bismuth titanate microspheres: directed synthesis and their visible light photocatalytic activity," *Applied Surface Science*, vol. 258, no. 18, pp. 7146–7153, 2012.
 - [13] V. Cloet, P. Lommens, R. Hühne, K. de Buysser, S. Hoste, and I. van Driessche, "A study of the parameters influencing the microstructure of thick La₂Zr₂O₇ films," *Journal of Crystal Growth*, vol. 325, no. 1, pp. 68–75, 2011.
 - [14] L. Li, X. Zhang, L. Ji, P. Ning, and Q. Liao, "Dielectric properties and electrical behaviors of tunable Bi_{1.5}MgNb_{1.5}O₇ thin films," *Ceramics International*, vol. 38, no. 5, pp. 3541–3545, 2012.
 - [15] C. S. Rastomjee, R. S. Dale, R. J. Schaffer et al., "An investigation of doping of SnO₂ by ion implantation and application of ion-implanted films as gas sensors," *Thin Solid Films*, vol. 279, no. 1-2, pp. 98–105, 1996.
 - [16] C. A. Mims, A. J. Jacobson, R. B. Hall, and J. T. Lewandowski, "Methane oxidative coupling over nonstoichiometric bismuth-tin pyrochlore catalysts," *Journal of Catalysis*, vol. 153, no. 2, pp. 197–207, 1995.
 - [17] A. Ratna Phani, S. Manorama, and V. J. Rao, "Effect of additives on the response of sensors utilizing semiconducting oxide on carbon monoxide sensitivity," *Applied Physics Letters*, vol. 66, no. 25, pp. 3489–3491, 1995.
 - [18] Q. Tian, J. Zhuang, J. Wang, L. Xie, and P. Liu, "Novel photocatalyst, Bi₂Sn₂O₇, for photooxidation of As(III) under visible-light irradiation," *Applied Catalysis A: General*, vol. 425–426, pp. 74–78, 2012.
 - [19] L. Moens, P. Ruiz, B. Delmon, and M. Devillers, "Evaluation of the role played by bismuth molybdates in Bi₂Sn₂O₇-MoO₃ catalysts used for partial oxidation of isobutene to methacrolein," *Applied Catalysis A: General*, vol. 180, no. 1-2, pp. 299–315, 1999.
 - [20] H. W. Kim, S. H. Shim, J. W. Lee et al., "Bi₂Sn₂O₇ nanoparticles attached to SnO₂ nanowires and used as catalysts," *Chemical Physics Letters*, vol. 456, no. 4–6, pp. 193–197, 2008.
 - [21] J. Wu, F. Huang, X. Lü, P. Chen, D. Wan, and F. Xu, "Improved visible-light photocatalysis of nano-Bi₂Sn₂O₇ with dispersed s-bands," *Journal of Materials Chemistry*, vol. 21, no. 11, pp. 3872–3876, 2011.
 - [22] J. Yang, J. Dai, and J. Li, "Synthesis, characterization and degradation of Bisphenol A using Pr, N co-doped TiO₂ with highly visible light activity," *Applied Surface Science*, vol. 257, no. 21, pp. 8965–8973, 2011.
 - [23] H. X. Shi, T. Y. Zhang, T. C. An et al., "Enhancement of photocatalytic activity of nano-scale TiO₂ particles co-doped by rare earth elements and heteropolyacids," *Journal of Colloid and Interface Science*, vol. 380, no. 1, pp. 121–127, 2012.
 - [24] V. Stengl, S. Bakardjieva, and N. Murafa, "Preparation and photocatalytic activity of rare earth doped TiO₂ nanoparticles," *Materials Chemistry and Physics*, vol. 114, no. 1, pp. 217–226, 2009.
 - [25] S. X. Wu, J. Z. Fang, X. X. Xu et al., "Microemulsion synthesis, characterization of highly visible light responsive rare earth doped Bi₂O₃," *Photochemistry and Photobiology*, vol. 88, no. 5, pp. 1205–1210, 2012.
 - [26] X. Z. Ding and X. H. Liu, "Correlation between anatase-to-rutile transformation and grain growth in nanocrystalline titania powders," *Journal of Materials Research*, vol. 13, no. 9, pp. 2556–2559, 1998.
 - [27] M. Ge, Y. F. Li, L. Liu et al., "Bi₂O₃–Bi₂WO₆ composite microspheres: hydrothermal synthesis and photocatalytic performances," *The Journal of Physical Chemistry*, vol. 115, no. 13, pp. 5220–5225, 2011.
 - [28] Y. C. Zhang, Z. N. Du, K. W. Li, and M. Zhang, "Size-controlled hydrothermal synthesis of SnS₂ nanoparticles with high performance in visible light-driven photocatalytic degradation of aqueous methyl orange," *Separation and Purification Technology*, vol. 81, no. 1, pp. 101–107, 2011.
 - [29] M. Takeuchi, Y. Shimizu, H. Yamagawa, T. Nakamuro, and M. Anpo, "Preparation of the visible light responsive N³-doped WO₃ photocatalyst by a thermal decomposition of ammonium paratungstate," *Applied Catalysis B: Environmental*, vol. 110, no. 2, pp. 1–5, 2011.
 - [30] A.-W. Xu, Y. Gao, and H.-Q. Liu, "The preparation, characterization, and their photocatalytic activities of rare-earth-doped TiO₂ nanoparticles," *Journal of Catalysis*, vol. 207, no. 2, pp. 151–157, 2002.

- [31] K.-I. Ishibashi, A. Fujishima, T. Watanabe, and K. Hashimoto, "Detection of active oxidative species in TiO_2 photocatalysis using the fluorescence technique," *Electrochemistry Communications*, vol. 2, no. 3, pp. 207–210, 2000.
- [32] S. X. Wu, J. Z. Fang, W. C. Xu et al., "Hydrothermal synthesis, characterization of visible-light-driven $\alpha\text{-Bi}_2\text{O}_3$ enhanced by Pr^{3+} doping," *Journal of Chemical Technology and Biotechnology*, vol. 2013, 8 pages, 2013.
- [33] Q. Xiang, J. Yu, and P. K. Wong, "Quantitative characterization of hydroxyl radicals produced by various photocatalysts," *Journal of Colloid and Interface Science*, vol. 357, no. 1, pp. 163–167, 2011.
- [34] Y. Yang, G. Zhang, and W. Xu, "Facile synthesis and photocatalytic properties of $\text{AgAgClTiO}_2/\text{rectorite}$ composite," *Journal of Colloid and Interface Science*, vol. 376, no. 1, pp. 217–223, 2012.
- [35] K. Ebitani, Y. Hirano, and A. Morikawa, "Rare earth Ions as heterogeneous photocatalysts for the decomposition of dinitrogen monoxide (N_2O)," *Journal of Catalysis*, vol. 157, no. 1, pp. 262–265, 1995.
- [36] X. Yan, J. He, D. G. Evans, X. Duan, and Y. Zhu, "Preparation, characterization and photocatalytic activity of Si-doped and rare earth-doped TiO_2 from mesoporous precursors," *Applied Catalysis B: Environmental*, vol. 55, no. 4, pp. 243–252, 2005.
- [37] J. K. Reddy, B. Srinivas, V. D. Kumari et al., " Sm^{3+} -doped Bi_2O_3 photocatalyst prepared by hydrothermal synthesis," *Chem-CatChem*, vol. 3, no. 2, pp. 360–364, 2009.



Hindawi

Submit your manuscripts at
<http://www.hindawi.com>

